Title

Quantitative Decoupling of Oxygen-Redox and Manganese-Redox Voltage Hysteresis in a Cation-Disordered Rock Salt Cathode

Permalink

Journal

ISSN

Authors

Huang, Tzu-Yang
Cai, Zijian
Crafton, Matthew J
et al.

Publication Date

DOI

Copyright Information

Peer reviewed

Quantitative Decoupling of Oxygen-Redox and Manganese-Redox Voltage Hysteresis in a Cation-Disordered Rock Salt Cathode

Tzu-Yang Huang, Zijian Cai, Matthew J. Crafton, Lori A. Kaufman, Zachary M. Konz, Helen K. Bergstrom, Elyse A. Kedzie, Han-Ming Hao, Gerbrand Ceder, Bryan D. McCloskey*

Zijian: DRX synthesis and carbon shaker-mill, material properties and redox mechanisms consult
Matt: DEMS/TiMS/calibration setup and design, DRX capacity-account consult
Lori: DEMS/TiMS/calibration setup, general cathode chemistries consult
Zach: Swagelok cell holder setup in constant-temp oven for GITT measurement
Helen: High-power LEDs setup help
Elyse: General O-redox chemistry consult, help discover photon-catalyzed oxalate reactions
Han-Ming: DRX synthesis help

T.-Y. Huang, M. J. Crafton, L. A. Kaufman, Z. M. Konz, H. K. Bergstrom, E. A. Kedzie, B. D. McCloskey
Department of Chemical and Biomolecular Engineering
University of California-Berkeley
Berkeley, CA 94720, USA
Email Address: bmcclosk@berkeley.edu

T.-Y. Huang, M. J. Crafton, L. A. Kaufman, Z. M. Konz, H. K. Bergstrom, E. A. Kedzie, B. D. McCloskey
Energy and Distributed Resources Division
Lawrence Berkeley National Laboratory
Berkeley, CA 94720, USA

Z. Cai, H.-M. Hao, G. Ceder
Department of Materials Science and Engineering
University of California-Berkeley
Berkeley, CA 94720, USA

Z. Cai, H.-M. Hao, G. Ceder
Materials Sciences Division
Lawrence Berkeley National Laboratory
Berkeley, CA 94720, USA

Abstract

Pronounced voltage hysteresis is commonly associated with oxygen redox in Li-excess cathode materials. However, they oftentimes involve coexisting transition-metal and oxygen redox, whose contributions to hysteresis are challenging to distinguish. In this work, a two-step aqueous redox titration was developed with the aid of mass spectrometry (MS) gas analyzer to quantify two coexisting solid-phase analytes, namely oxidized oxygen and $Mn^{3+/4+}$, in a representative Li-excess cation-disordered rock salt — $Li_{1.2}Mn_{0.4}Ti_{0.4}O_2$ (LMTO). Two MS-countable gas molecules evolve from two separate titrant-analyte reactions, which allows decoupling Mn and O redox capacities. Along the capacity dimension, LMTO cathode displays unforeseen reversibility with each redox coulombic efficiencies close to 100%, as well as reversible faradaic selectivity between two mixed redox mechanisms. As incremental redox capacities are quantitatively decoupled, each redox voltage hysteresis can be further evaluated through deconvoluted energy efficiency and overvoltages. Overall, LMTO voltage hysteresis arises not only from intrinsic charge-discharge voltage mismatch of O redox, but also from asymmetric Mn-redox overvoltages. The results reveal that O redox is not always the only culprit for pronounced voltage hysteresis and slow kinetics, but instead discharging overvoltage, associated with transition-metal redox, can significantly drag down overall energy efficiency. This work further shows the potential of designing new analytical workflow to experimentally tease out key missing properties, even in a disordered material having complex local coordination environments.

1 Introduction

In the global movement toward electrifying transportation, three of determinants for viable electric-vehicle (EV) batteries are cell cost, energy density, and energy efficiency. These three factors are governed mostly by the cathode materials for common Li-ion batteries.[1] As the cell cathode in booming EV market is dominated by stoichiometric layered chemistries ($LiMO_2$, M = Ni, Co, Mn, Al), limited cobalt and nickel resources[2,3] have raised concern over impending supply disruptions that can result in cell cost volatility.[4] Adopting low-cost and sustainable raw materials for cathodes in Li-ion batteries has become particularly important for ongoing research and development. One prominent type of emerging cathode materials is Li-excess cation-disordered rock salt (DRX),[5–7] because it can accommodate diverse earth-abundant transition-metal (TM) chemistries such as Mn and Ti [8,9] while at the same time exhibiting high gravimetric energy densities that approach 1000 Wh kg^{-1}.[10] Despite their high energy densities achieved with low-cost resources, DRX materials' inherent cation site mixing not only induces non-uniform Li site energies[11], but also activates coexisting TM-redox and oxygen-redox charge compensation mechanisms.[12–14] Synergistically, these diverse characteristics among DRX materials lead to dissimilar voltage profiles, as well as varying gaps between charge and discharge curves.[6,15] The resulting charge-discharge voltage curves mismatch, commonly termed voltage hysteresis, diminishes DRX cathodes' operating energy efficiency.

Voltage hysteresis can be clearly visualized by plotting charging and discharging voltage V against cumulative capacity q, which is defined here as the net amount of electron transferred from the cathode to the external circuit, where incremental electric charge $dq > 0$ on charging (Chg) and $dq < 0$ on discharging ($Dchg$):

$$q = \int_{Chg} dq + \int_{Dchg} dq \tag{1}$$

At a definite voltage V, incremental capacity dq is measurable by a potentiostat, but dq is ultimately redistributed and compensated by a set of redox-active species, denoted with i, such as TM and O in the DRX material:

$$dq = \sum_i dq_i \tag{2}$$

Among various redox-mechanism studies, recent spectroscopic and ab initio research have provided tantalizing evidence correlating voltage hysteresis with oxygen redox that may entail different oxidized oxygen species formation (e.g., trapped O_2 [13,16] or non-dimerized O^- [17,18]) as well as varying local

coordination (e.g., TM migration,[12, 19, 20] defect formation,[21] or ligand-to-metal charge transfer[22]). However, few studies can experimentally decouple and quantify capacities with mixed contribution from both TM redox and O redox. Quantitative distribution of dq_i in Equation (2) is challenging to measure by either spectroscopy or a potentiostat, because an exact same voltage level can involve more than one charge compensation mechanism. Therefore, dq_i remains a critical piece of missing information for studying and improving voltage hysteresis. As voltage mismatch varies across the capacity axis, dissimilar dq_i history of each redox process i implicates different round-trip energy efficiency η_i:

$$\eta_i = \frac{-\int_{Dchg} V dq_i}{\int_{Chg} V dq_i} \tag{3}$$

In other words, acquiring deconvoluted energy efficiency η_i will allow us to evaluate how each redox mechanism i impacts voltage hysteresis, once we resolve key unknowns — decoupled capacities dq_i.

To address this challenge, we first re-designed conventional aqueous redox titration with the aid of mass spectrometry (MS) gas analyzer to quantify the amount of solid-phase oxidized oxygen and $Mn^{3+/4+}$ individually within a representative Mn-based DRX material, $Li_{1.2}Mn_{0.4}Ti_{0.4}O_2$. Two-step titration induces two distinguishable gas molecules, which are quantifiable by MS gas analyzer. As reaction stoichiometry is linear in each step, we can backcalculate Mn-redox and O-redox capacities, separately. Next, we measured voltages at a constant current, as well as quasi-equilibrium states. Deconvoluted voltage hysteresis was presented by plotting voltages against decoupled capacities. At the end of this work, redox hysteresis curves enable us to decouple redox energy efficiencies, as well as redox overvoltage distribution, which unambiguously inform how different each redox mechanism contributes to the overall voltage hysteresis. Our results show promise of designing new analytical workflows to experimentally tease out key missing properties, even in a DRX material having complex local coordination environments. Thus, we anticipate that our titration design strategies can be further extended to other cathode chemistries involving mixed transition-metal and oxygen redox.

2 Results and Discussion

## 2.1 Titration Design by Analyte's Aqueous Instability

Conventional aqueous redox titration, such as iodometric titration, was designed on the basis of fast (in few seconds) electron-transfer reactions between titrant and analyte solution in a single-phase liquid environment. To quantify oxidant analytes in solid phase — i.e., oxidized oxygen and $Mn^{3+/4+}$ in the DRX material — adopting regular redox titration is oftentimes challenging due to $Mn^{3+/4+}$-containing oxide materials' low aqueous solubility, where slow heterogeneous reaction kinetics between solid analyte and liquid titrant becomes susceptible to interference by other non-negligible side reactions (e.g., ambient air slowly oxidizes iodide in iodometry[23]). In light of the limitation described above, we re-examined the adjustable solution chemistry by blending appropriate titrants to effectively destabilize each solid-phase analyte under specific aqueous conditions, which promotes analytes' disintegration accompanied with characteristic gas release as detailed in the following sections.

2.1.1 Frost Diagram

Solid-phase oxidized oxygen species existing in TM oxides have been shown unstable with substantial O_2 gas release in strong aqueous acid,[24, 25] when concentrated proton H_3O^+ replaces mobile lattice Li^+.[26] This self-decomposition is well predicted by aqueous thermodynamic stability of the oxygen element with various formal oxidation numbers N, which can be further visualized by a Frost diagram[27] plotting free energies (N multiplied by electrochemical potential relative to O_2) of different oxidation states shown in **Figure 1a**. If three participating states form a concave-down connection in **Figure 1a** (e.g., $H_2O \leftarrow H_2O_2 \rightarrow O_2$), disproportionation of a certain state into two neighboring states, where net change of N in both positive and negative directions equals zero, is thermodynamically favorable. Ultimately, regardless of oxidation numbers, aqueous oxidized oxygen species are prone to disproportionate all the way into end members H_2O and O_2.

The thermodynamic instability predicted by the Frost diagram is applicable to oxidized oxygen existing in a solid DRX material because we have previously used an oxygen isotope to study ^{18}O-enriched DRX material and unambiguously shown that DRX-derived O_2 gas release during strong acid titration can accurately estimate oxygen-redox capacity.[28] The backcalculation is based on the following two equations, where other elements (Li and TM) in the DRX solid are not shown in formula

for clarity and the electrochemical cell hosts the initial electron-transfer reaction:

$$2\,O^{2-}(s) \xrightleftharpoons[DChg]{Chg} 2\,O^{n-}(s) + 2(2-n)\,e^- \tag{4}$$
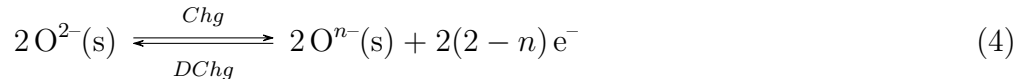
Here two O^{n-} (s) can be either dimerized or non-dimierized. We posit that with strong aqueous acid infused during the titration, relaxed O^{n-} in aqueous environment preferentially dimerize due to closer frontier-orbital energy and symmetry match,[29] which is followed by disproportionation-O_2 release from the ex-situ cathode:

$$2\,O^{n-}(s) + 2n\,H_3O^+(aq) \xrightarrow{aqueous\ acid} 3n\,H_2O(l) + \frac{2-n}{2}\,O_2(g) \tag{5}$$
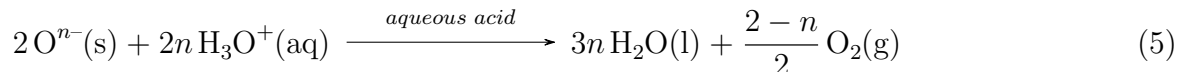
Therefore, cumulative O-redox capacity $2(2-n)$ is linearly correlated with acid-induced O_2 quantity. Moreover, their linear relationship is independent of formal oxidation state $n-$, (O-capacity divided by O_2 quantity is invariant, $2(2-n)\cdot(\frac{2-n}{2})^{-1} = 4$) which allows quantification of solid-phase oxidized oxygen from Equation (4) with any n in $0 \leq n < 2$. The wide-range applicability further suggests that our titration design is generizable for quantifying O-redox capacity originating from various oxidized oxygen species in solid phase.

2.1.2 Pourbaix Diagram

Solid-aqueous equilibria predict solid materials' stability (corrosion or passivation) in various aqueous environment, where thermodynamically the most stable phases at a given pH value and applied potential can be displayed on a Pourbaix diagram.[30] To access $Mn^{3+/4+}$ within the bulk of solid DRX materials in our titration design, titrant solution must be optimized to effectively disintegrate solid DRX analyte into soluble aqueous forms. Here we first analyzed a Pourbaix diagram for cation-ordered spinel $LiMn_2O_4$ in **Figure 1b** (see Experimental Section for computation details[31–33] generating the plot) and we anticipated that $LiMn_2O_4$-aqueous equilibria analysis is applicable to the DRX material $Li_{1.2}Mn_{0.4}Ti_{0.4}O_2$ having more complex cation disorder, because redox-active Mn in the DRX material possesses similar oxidation states with octahedral coordination to rock-salt-like anion lattice as Mn in $LiMn_2O_4$.

When spinel $LiMn_2O_4$ is immersed in the acid titrant with trace O_2, creating an aqueous environment with pH ≈ 0 and $\sim$1.20 V of H_2O/O_2 equilibrium potential applied near $LiMn_2O_4$ surface, as labelled by the grey diamond marker in **Figure 1b**, the initial state holding solid-phase $Mn^{3+/4+}$ is

prone to transform into aqueous Li^+ and Mn^{2+}. However, instead of forming fully transparent solution, experimentally the spinel manganese oxide remains in undissolved and dispersed solid phase, as shown by **Figure S1a** in Supporting Information (SI). This result agrees with material's low thermodynamic
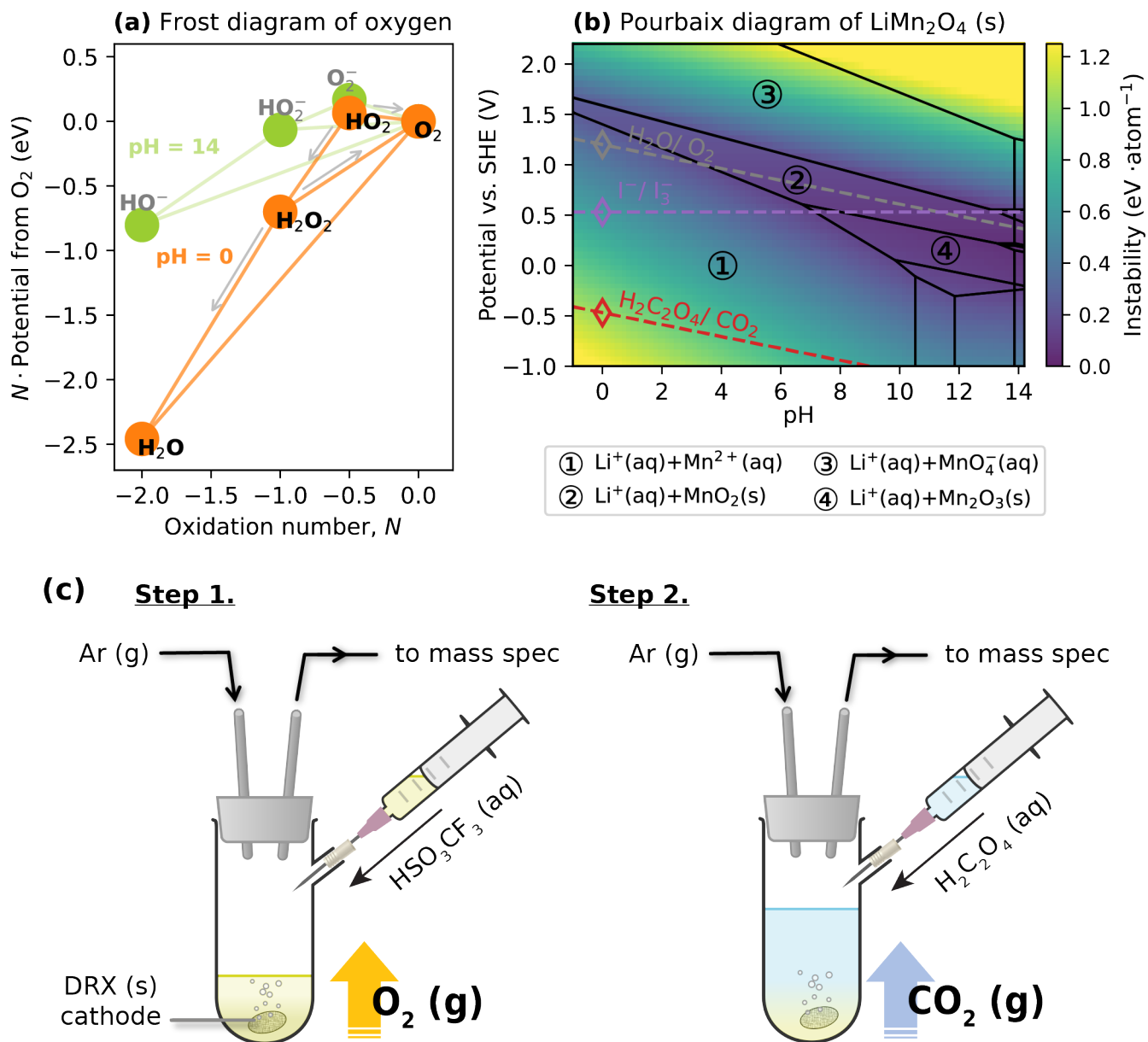

Figure 1: Two-step titration design by analyte's aqueous instability. (a) Oxygen Frost diagram in basic and acidic aqueous solution. Formal oxidation number N of oxygen varies horizontally, while the vertical axis presents N multiplied by standard half-reaction potential between each state and O_2. (b) Li-Mn-O-H Pourbaix diagram overlaid with $LiMn_2O_4$ instability map. The diagram is generated computationally, as described in Experimental Section. (c) Illustration of two-step titration mass spectrometry and its experimental setup. Strong aqueous acid HSO_3CF_3 (triflic acid) destabilizes solid-phase oxidized oxygen upon the first injection. The second injection involves reaction between solid-phase $Mn^{3+/4+}$ and oxalic acid, which produces CO_2. Characteristic O_2 or CO_2 released from each analyte-titrant reaction is quantifiable by the mass-spectrometry gas analyzer.

instability that can be measured by a computed relative free energy map,[32] as displayed at the grey diamond marker in **Figure 1b**: 0.30 eV atom^{-1}. In addition, during H_2SO_4 acid titration, we did not observe water-splitting O_2 gas ($2H_2O$ (l) $\rightarrow O_2$ (g) $+ 4H^+ + 4e^-$, SI **Figure S2a**), which should be the most probable aqueous charge-compensating redox couple[28] for $Mn^{3+/4+}$ reduction without external circuit. No water-derived O_2 release indicates no decomposition reaction involving non-zero net electron transfer to solid-phase $Mn^{3+/4+}$ (e.g., Mn^{3+} (s) $+ e^- \rightarrow Mn^{2+}$ (aq)). Therefore, to decompose and reduce solid-phase $Mn^{3+/4+}$, the acid titrant must be adjusted to a different aqueous condition that promotes solid-phase thermodynamic instability.

Along the vertical axis of relative free energy map, lowering aqueous equilibrium potential near solid oxide surface is clearly the most effective way to push the initial solid phase towards higher instability, as shown in **Figure 1b** by moving the diamond marker downwards to the brighter region. Naturally we introduced an aqueous reductant, oxalic acid, to effectively lower the applied aqueous equilibrium potential. Here the specific reductant was selected instead of regular redox titrant such as potassium iodide, because our titration design requires several titrant properties possessed by aqueous $H_2C_2O_4$. First, low equilibrium potential of aqueous $H_2C_2O_4$ adequately enhances the thermodynamic instability of liquid-surrounded $LiMn_2O_4$. While conventional redox titrant with I^-/I_3^- entails $LiMn_2O_4$ instability at 0.59 eV atom^{-1} larger than 0.30 eV atom^{-1} by H_2O/O_2 under acid condition (**Figure 1b**), oxalic acid titrant with $H_2C_2O_4/CO_2$ ramps up the instability to 1.02 eV atom^{-1}. Second, $H_2C_2O_4$ redox titration product is CO_2 in the gas phase, which can be easily separated from the analyte-titrant mixture and thus is reliably quantifiable. Removed CO_2 gas from the solution also ensures titration to a greater extent of reaction, following Le Chatelier's principle. Third, carbon atoms in the redox couple $H_2C_2O_4/CO_2$ carry explicit formal charges, which warrants unambiguous charge-compensation stoichiometry. Unlike other organic acid candidates such as citric acid, change of carbon oxidation states from $H_2C_2O_4$ (3+) to CO_2 (4+) is readily trackable. Overall, oxalic acid's unique characteristics listed above make it exceptionally suitable for quantifying solid-phase $Mn^{3+/4+}$.

The stoichiometric relation can be clarified via the following two equations, where electron transfer is first measured in an electrochemical cell, and y is a constant (fixed for each material) defined as the pristine number of Mn^{3+} per unit formula:

$$\text{Mn}_y^{3+}(\text{s}) \xrightleftharpoons[DChg]{Chg} \text{Mn}_y^{(3+\frac{m}{y})+}(\text{s}) + m\,\text{e}^- \tag{6}$$
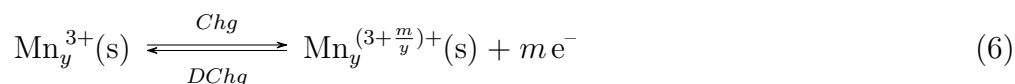
For clarity of Equation (6), we do not show other elements (Li and O) in the solid material. Here solid-phase $Mn^{3+/4+}$ reacts with $H_2C_2O_4$ to release CO_2 gas when ex-situ cathode is titrated:

$$Mn_y^{(3+\frac{m}{y})+}(s) + \frac{m+y}{2} H_2C_2O_4(aq) \longrightarrow (m+y) H^+(aq) + y Mn^{2+}(aq) + (m+y) CO_2(g) \qquad (7)$$
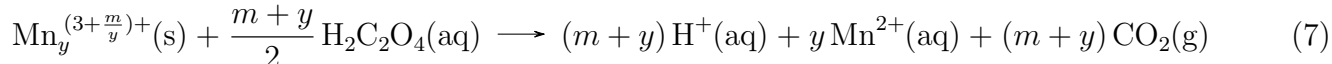
Cumulative Mn-redox capacity varies linearly with the amount of oxalate-derived CO_2, ($q_{Mn} = m$; $q_{Mn} = CO_2 - y$) which completely agrees with our titration experiments on the spinel $LiMn_2O_4$ cathode. (See SI **Figure S2**) Such experimental agreement with backcalculation shows promise of quantifying Mn-capacity, particularly in the Mn-based DRX material going forward, by our oxalic-acid titration design.

2.1.3 Two-Step Titration Mass Spectrometry (TiMS)

Disproportionation-O_2 and oxalate-CO_2 release processes during titration are intended for solid-phase oxidized oxygen and $Mn^{3+/4+}$, separately. To individually quantify O-redox and Mn-redox capacities, aqueous environment surrounding ex-situ DRX cathode must be controlled to avoid crossover interference. Namely, preventable errors might still take place if unintended reactions, such as $O^{n-} + H_2C_2O_4$, were not restrained. In pursuing well-controlled aqueous conditions for quantifying co-existing solid analytes in two distinct reactions, we titrated each extracted cathode with sequential injections in two steps. The first injection involved strong aqueous acid infusion into the ex-situ DRX cathode, which destabilizes solid-phase oxidized oxygen species and releases associated O_2 gas. Besides oxidized oxygen as the first major analyte, surface carbonate-like side products were fully decomposed in strong acid and emitted carbonate-CO_2 gas.[34] Both carbonate-CO_2 and disproportionation-O_2 were continuously counted and removed (**Figure 1c**) until complete attenuation, which minimizes the amount of carbonate and oxidized oxygen left for the following step. Next, as shown in **Figure 1c**, oxalic acid was injected to reductively decompose remaining $Mn^{3+/4+}$ in the solid oxide, which releases oxalate-CO_2 downstream in this second step. As a result of our two-step titration design, we limit the crossover interference between two major analyte-titrant reactions, which more strictly decouples two redox capacities as calculated from disproportionation-O_2 and oxalate-CO_2.

To distinguish and account each characteristic gas molecule accurately, we attached our titration vessel to a gas-handling system equipped with a quadrupole mass spectrometer.[28] Due to MS gas analyzer's high sensitivity, it is suitable to quantify dilute molecules in the head-space gas mixture, (detection limit $\geq$ 0.02 mol%) which also helps determine the end of each titration step through

attenuating gas of interest. Moreover, if any unexpected gas (other than O_2 and CO_2) evolved during titration, our MS gas analyzer with adequate molar-mass resolution can readily detect and identify any possible side reactions. Indicators of side reactions are crucial at the early stage of our titration design, because these side reactions are likely to introduce interference. For example, over 100% yield of oxalate-CO_2 accompanied nitrogen monoxide gas release when second-step oxalic acid mixed with first-step concentrated HNO_3 titrant. In this case nitrate anion was obviously the source of the unintended NO gas, which directs us to modify strong acid chemistry with other anions compatible with aqueous oxalic acid. Triflic acid (HSO_3CF_3 (aq)) was selected as the strong acid titrant, due to its extremely negative pKa and its stable anion chemistry. See SI **Note S2** and **Figure S4, S5** for details of optimizing $Mn^{3+/4+}$-oxalate reaction conditions with the aid of our MS gas analyzer. To sum up, mass spectrometry combined with two-step titration design (TiMS) enables us to identify and remove potential sources of interference, which warrants accurate quantification of both characteristic gas molecules and backcalculated capacities.

2.2   Decoupling Mixed Redox Capacities

Coexisting Mn and O redox have been shown as the major charge compensation mechanisms[15] in our DRX material $Li_{1.2}Mn_{0.4}Ti_{0.4}O_2$ (LMTO; SI **Figure S3**). For Mn-based DRX materials undergoing first charge, each redox capacity is challenging to quantify independently at higher states of charge (SOC), because high-voltage side reactions complicate any decoupling effort with parasitic capacity contribution from the cathode-electrolyte interface[25] (all side reactions other than Mn and O redox, $dq_{side} \neq 0$). Here we first avoided parasitic reactions by running LMTO within a shallow SOC range, ($y = 0.4$ and $0 \leq m \leq 0.3$ in Equation (6), (7)) as displayed in **Figure 2a**. The voltage profile lays out upper capacity axis in a molar electric charge unit, mol e mol^{-1} (moles of electrons per mole of active material LMTO), because in this work we mostly adjust SOC by $dq = 0.1$ mol e mol^{-1} (32.9 mAh g^{-1}) to study LMTO cathodes at different SOC. In the low capacity range, our differential electrochemical mass spectrometry (DEMS) shows small in-situ CO_2 evolved from interface degradation processes, (< 2 mmol mol^{-1}, SI **Figure S6a**) which indicates negligible parasitic capacity contribution. In addition to limited side reactions, there is minimal O-redox activity: neither in-situ gaseous O_2 loss (SI **Figure S6a** by DEMS) nor solid-phase oxidized oxygen (**Figure 3a** by TiMS) in the shallow SOC range. Therefore, the low-SOC capacity essentially represents pure Mn-redox capacity, (measurable by a potentiostat, $q = q_{Mn}$) which is linearly correlated with TiMS oxalate-CO_2, as displayed in **Figure 2b, c**.
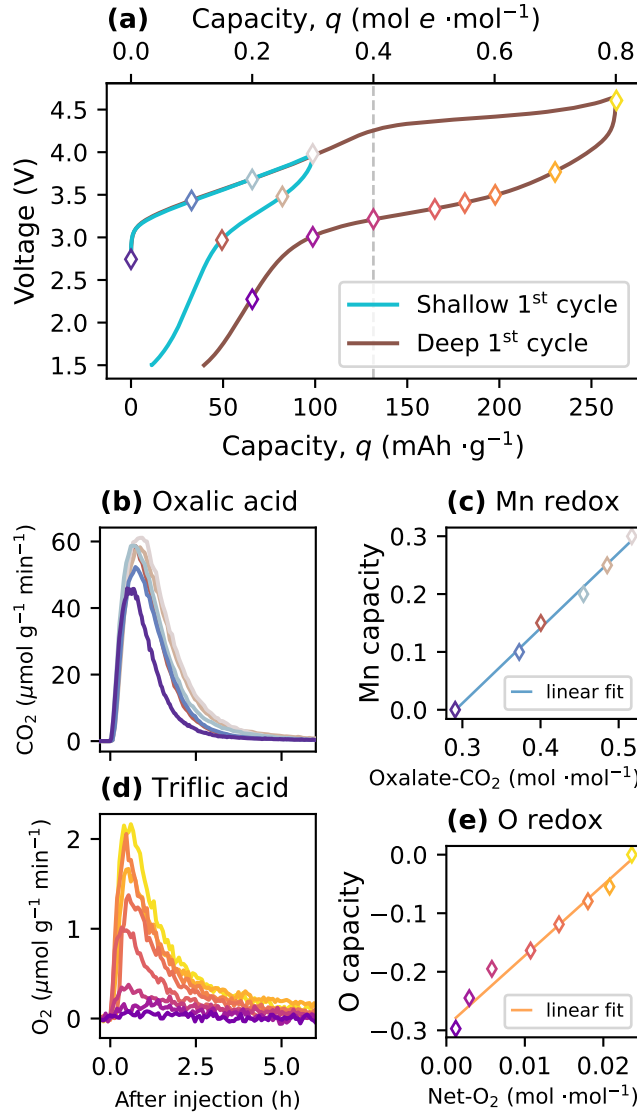
Figure 2: Capacity decoupling for cation-disordered rock salt $Li_{1.2}Mn_{0.4}Ti_{0.4}O_2$ (LMTO) via titration mass spectrometry (TiMS). (a) First-cycle voltage profiles of LMTO. The vertical dashed line marks the expected maximum Mn capacity. Diamond markers denote cathode extraction from various cells at different state of charge. (b) Oxalate-CO_2 evolution curves from applying 2-step TiMS on cathodes cycled within the first shallow cycle. (c) Linear regression between shallow-cycle Mn capacity and oxalate-CO_2: $q_{Mn} = 1.2993 \cdot CO_2 - 0.3786$; $R^2 = 0.9944$. Data points are color-coded to match pure Mn capacities in Figure 2a and TiMS CO_2 curves in Figure 2b. (d) Acid-O_2 evolution curves from applying 2-step TiMS on cathodes discharged within the first deep cycle. (e) Linear regression between discharge O capacity and acid-O_2: *Dichg* $q_O = 12.079 \cdot O_2 - 0.2932$; $R^2 = 0.9799$. Discharge O capacities were derived from Equation (8), where interface parasitic reaction contribution is negligible. Data points are color-coded to match extraction states in Figure 2a and TiMS O_2 curves in Figure 2d.

Oxalate-CO_2 linear regression is useful to predict Mn-redox capacity q_{Mn} over the entire SOC range with mixed redox contribution, because our two-step titration and backcalculation intrinsically limit crossover interference from the other major capacity contribution — O redox.

To extract O capacity from any SOC range with mixed redox contribution, we turned to various discharge states, after charging LMTO cathodes to an identical delithiation state (0.8 Li^+ removed per unit LMTO, **Figure 2a**). Because cathode-electrolyte interface degradation has been identified mostly during high-voltage charge,[35–37] we cut down intermixed redox components by assuming negligible parasitic contribution during first discharge ($dq_{side} = 0$ in Equation (2)). In other words, discharge O capacity can be derived from potentiostat-measurable net discharge capacity and oxalate-measurable Mn capacity:

$$\int\limits_{Dchg} dq_O = \int\limits_{Dchg} dq - \int\limits_{Dchg} dq_{Mn} \tag{8}$$

Between the extracted O capacity and disproportionation-O_2, there is a clear linear correlation shown in **Figure 2d, e**. Here disproportionation-O_2 linear regression is applicable to other SOC range over the entire charge-discharge cycle, due to analogous reasoning for oxalate-CO_2. As a result, each characteristic gas from TiMS has its own refined linear correlation with the corresponding redox capacity in LMTO, which further enables capacity decoupling in any SOC range and cycle.

2.2.1 First-Cycle Redox Components

The first cycle of LMTO shows a different voltage profile among three initial slow-rate cycles, commonly called formation process, (SI **Figure S7**) as both DRX bulk[12] and surface[25,38] change lastingly. To clearly capture this change in terms of redox contribution, here we present first-charge and first-discharge data separately in **Figure 3** by laying out decoupled capacities q_i vs. net capacity q. Although q_i data are discrete in our method, we believe that the dq_i size is adequate for numerical integration and differentiation, which provides accurate approximation with a reasonable lab-scale throughput. As displayed by orange markings in **Figure 3**, O-redox capacity was translated from TiMS disproportionation-O_2; blue markings indicate that Mn-redox capacity was calculated from oxalate-CO_2, which altogether visualize trends of decoupled capacities during first-cycle charge and discharge.

Upon charge, Mn capacity initially grows along the parity line (net capacity) in **Figure 3c**, until q_{Mn} hits 0.3 mol e mol^{-1}. Within the following SOC range of 0.3-0.5 mol e mol^{-1}, Mn redox becomes stagnant. The pause comes before Mn capacity reaches expected maximum (0.4 mol e mol^{-1}), which suggests that not all solid-phase Mn has been oxidized to 4+ state. Average Mn oxidation state remains around 3.68+ within this static-q_{Mn} range. Instead of growing Mn capacity after $q \geq 0.3$ mol e mol^{-1},

the parasitic capacity contribution starts increasing, which was evaluated through the other measurable capacities in Equation (2): $dq_{side} = dq - dq_{Mn} - dq_O$. As parasitic capacity builds up halfway along the static-q_{Mn} range ($q \geq 0.4$ mol e mol^{-1}), O-redox contribution begins, which indicates that solid-phase LMTO starts holding non-transient oxidized oxygen species. Later onset of q_O than q_{side} further implies that stable oxidized oxygen may require preceding surface passivation. Although surface parasitic capacity dominates in static-q_{Mn} range, q_{side} soon plateaus around 0.11 mol e mol^{-1} with following O capacity growth as well as Mn-redox revival. The last q_{Mn} growth ends near its expected maximum, while q_O increases steadily towards 0.29 mol e mol^{-1} at the end of first charge. Overall, our Mn capacity trend agrees with other research's ab initio calculation,[13] which presented Mn oxidation under similar DRX local coordination (**Figure 3c** in this work vs. Figure 4c in the reference[13]). Furthermore, another computational study has linked DRX material's O redox to Mn migration.[12] Although Mn migration is not favored by Mn^{4+} having large activation energy barrier to move out of octahedral ligand field,[39] our Mn-capacity accounting indicates that movable Mn^{3+} or Mn^{2+} exist at O-redox onset, which can support previous Mn-migration argument.[12] The validation suggests that our titration design is suitable to quantify Mn-redox capacity in DRX cathodes experimentally. In addition to TiMS experiments, our DEMS measurements reveal negligible in-situ O$_2$ gas loss ($<$ 0.5 mmol mol^{-1}, SI **Figure S6b**), which confirms that solid-phase oxidized oxygen prevails in O-redox capacity across high SOC range before turning to discharge.

For the first discharge within operating voltage window 4.55-1.50 V (**Figure 2a**), we present decoupled capacities along net discharge capacity ($Dchg\ q = \int_{Dchg} dq < 0$, **Figure 3f**). As discharge dq_{side} has been assumed negligible, net discharge capacity matches the sum of Mn and O capacities. Both redox mechanisms contribute across most of discharge SOC range, where their discharge combination is different from first-charge redox pattern. For example, static-q_{Mn} range spans 0.2 mol e mol^{-1} during first charge, while analogous static range is narrower ($-0.3 \leq Dchg\ q \leq -0.2$ mol e mol^{-1}) during discharge. Although discharge redox distribution does not mirror first charge, each individual Mn and O capacity has a round-trip coulombic efficiency (CE_i) close to 100%:

$$CE_i = \frac{-\int_{Dchg} dq_i}{\int_{Chg} dq_i} \tag{9}$$

This decoupling result in DRX cathodes is surprising, as fully reversing q_{Mn} and q_O is not required by
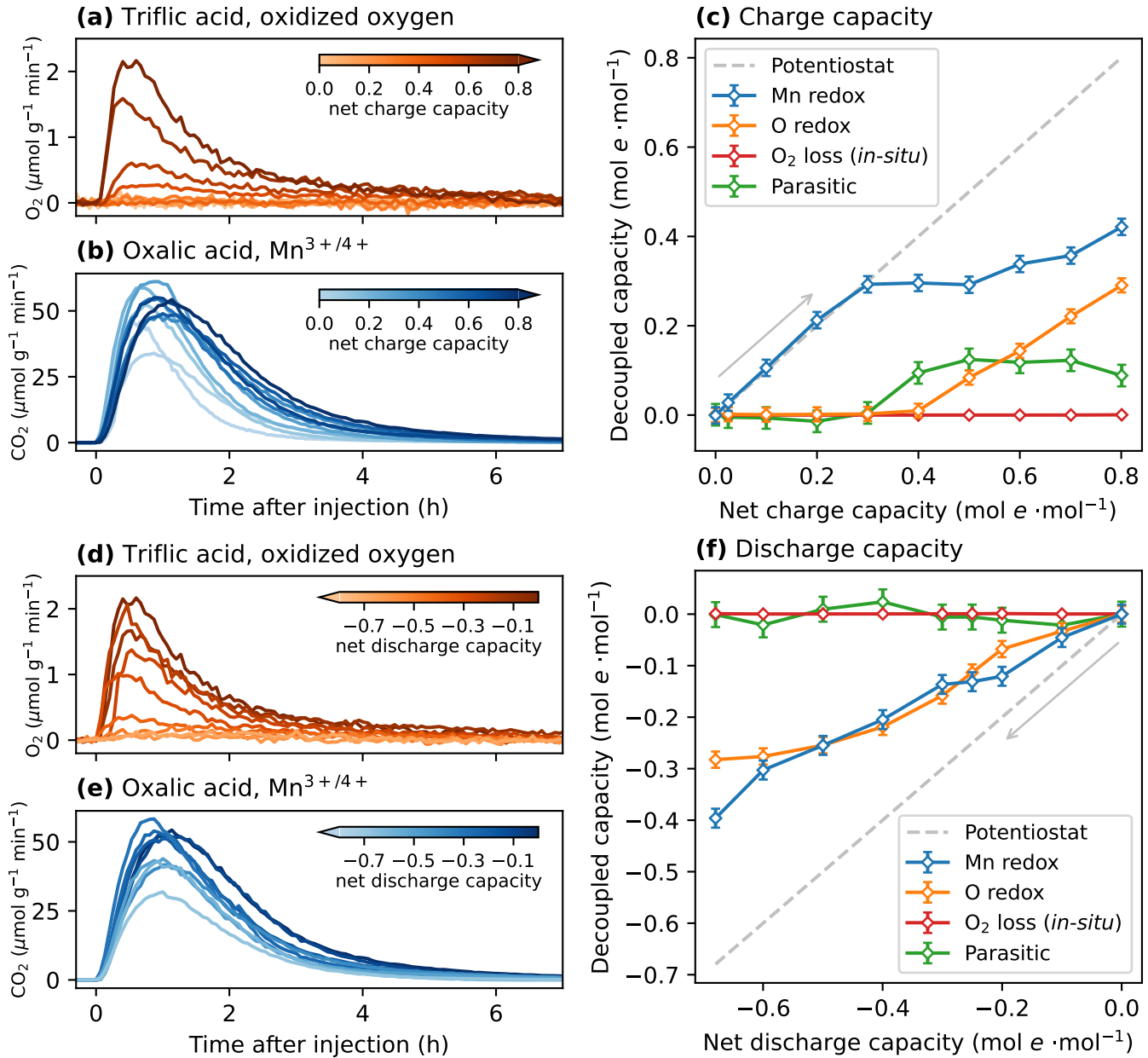
Figure 3: Firt-cycle redox components quantified via two-step titration. (a) O_2 evolution curves from the first injection on charged LMTO cathodes. (b) CO_2 evolution curves from the second injection on charged LMTO cathodes. (c) Decoupled charge capacities plotted against net charge capacities. In-situ O_2 loss was quantified by differential electrochemcal mass spectrometry (DEMS, SI Figure S6), and the backcalculated capacities follow 4 mol e per mol of O_2 loss. Interface parasitic capacities were derived from Equation (2): $dq_{side} = dq - dq_{Mn} - dq_O$. (d) O_2 evolution curves from the first injection on discharged LMTO cathodes. (e) CO_2 evolution curves from the second injection on discharged LMTO cathodes. (f) Decoupled discharge capacities plotted against net discharge capacities.

any of our method and underlying assumptions. Under the same TiMS method, spinel $LiMn_2O_4$ cathode shows irreversible q_{Mn} after first-discharge cutoff (**Figure S2b**), which agrees with other methods such as X-ray spectroscopy.[40] The experimental agreement not only validates our TiMS method again, but also suggests different irreversible-capacity origin between DRX and ordered cathode materials. In other

words, discharged ordered materials have residual oxidized TM left from incomplete lithiation,[40,41] which governs their first-cycle irreversible capacities. On the other hand, disordered LMTO's irreversible capacity is dominated by parasitic components ($q_{side} \approx 0.11$ mol e mol^{-1}), which implies that engineering the DRX-electrolyte interface promises to achieve a higher overall coulombic efficiency CE. To sum up, our decoupling technique reveals almost 100% reversible q_{Mn} and q_O, but their patterns are different for first charge and discharge, which is a contrast to the following cycle.

2.2.2 Second-Cycle Mn and O Redox: Reversible Faradaic Selectivity

To ensure all second-cycle LMTO cathodes underwent similar redox history, their first-cycle cutoff were set at identical capacities, (Chg $q = 0.8$ and $Dchg$ $q = -0.65$ mol e mol^{-1}) after which each second-cycle cathode was extracted within 4.55-1.50 V. **Figure 4** displays major redox capacities vs. net capacity cumulatively, where we zero cumulative capacities upon starting each cycle.

Upon second charge, Mn-redox capacity dominates shallow SOC range within $0 \leq q \leq 0.1$ mol e mol^{-1}, (**Figure 4b**) which reflects first-discharge tail range followed by the second cycle.
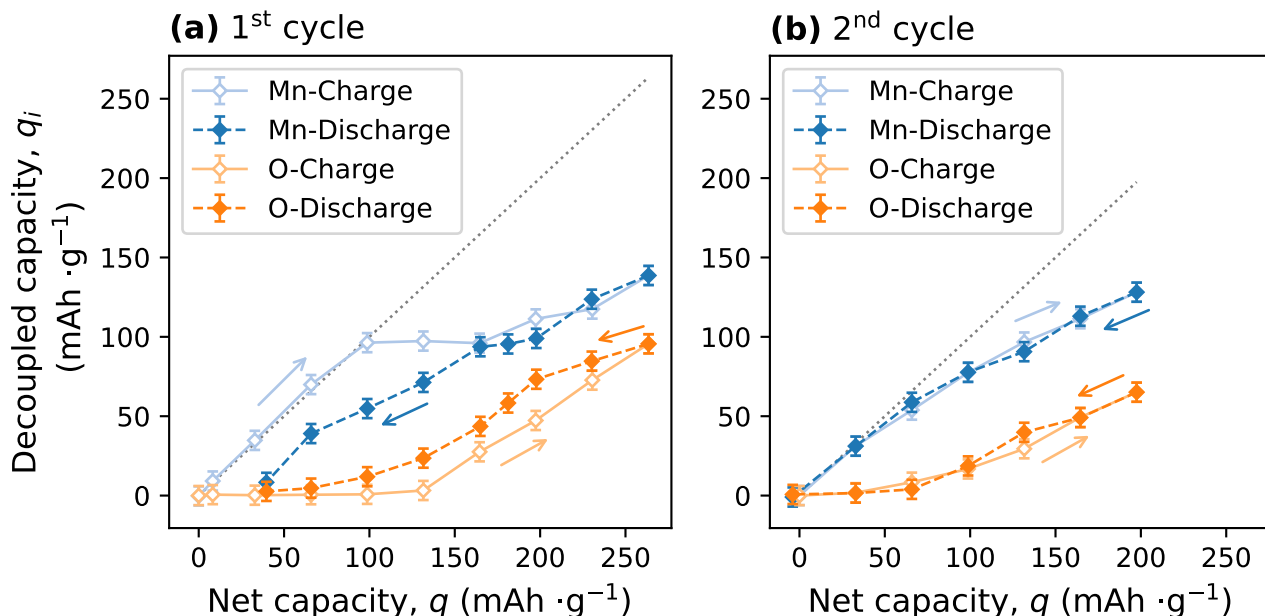

Figure 4: Redox combinations and their faradaic selectivity for LMTO cathodes. (a) First-cycle decoupled Mn-redox and O-redox capacities q_i plotted against net capacities q. As round-trip q_i ends near zero vertically, Mn and O capacities display decoupled coulombic efficiencies close to 100%, evaluated via Equation (9). (b) Second-cycle redox combinations. Beyond the first cycle, Mn and O redox not only uphold their reversibility in decoupled capacity q_i, but also develop reversible faradaic selectivity (S_i in Equation (10)) across the second cycle.

However, two cycles show dissimilar redox trends on charging, which implies that the first round-trip cycle does not push DRX electronic band structure[14, 42] back to its pristine state before the second cycle starts. In particular, second-charge q_{Mn} and q_O grow together over 0.5 mol e mol^{-1} of SOC range, while first charge only has 0.3 mol e mol^{-1} of co-developing range near cutoff. Turning to discharge, both cycles show Mn and O capacities with CE_i close to 100%, as round-trip q_i ends near zero vertically in **Figure 4**. Horizontally, net irreversible capacity creates a gap between zero and first-cycle endpoint q as a result of non-zero q_{side}, while second-cycle net capacity is fully compensated by q_{Mn} and q_O. In other words, parasitic contribution q_{side} becomes negligible at any second-cycle SOC based on Equation (2), which implies more stable DRX-electrolyte interface after the first formation cycle.

Beyond the first cycle, Mn and O redox not only uphold their reversibility in decoupled capacity q_i, but also develop reversible faradaic selectivity (S_i) across the second cycle:

$$S_i = \frac{dq_i}{dq} \tag{10}$$

Across horizontal q axis in **Figure 4b**, each cumulative q_i has discharging route overlaying charging curve, which indicates reversible S_i. That is, regardless of charging or discharging, as long as they proceed towards the same SOC, both second-cycle routes end with an identical electric-charge distribution between solid-phase Mn$^{3+/4+}$ and oxidized oxygen. The resolved redox trends implies less variable DRX band structure in the second cycle, as S_i becomes reversible. To summarize, redox-reaction reversibility is twofold in our DRX material: reversible Mn and O capacities, each with close to 100% coulombic efficiency in first two cycles; at any second-cycle SOC, faradaic selectivity is reversible, with charge-discharge path independence. Most importantly, these reversible properties are decoupled for Mn and O redox, which allows deconvolution of voltage hysteresis.

2.3 Deconvoluted Voltage Hysteresis

Up to now, we have decoupled LMTO's electrochemical properties mostly in the electric-charge dimension dq, which has not fully uncovered material hysteresis during energy storage and delivery. To access the energy scale of Mn and O redox, we must bring in another measurable quantity — voltage V. With voltages recorded under open circuit and closed circuit, our deconvoluted voltage hysteresis further distinguishes between intrinsic and operating energy efficiency.
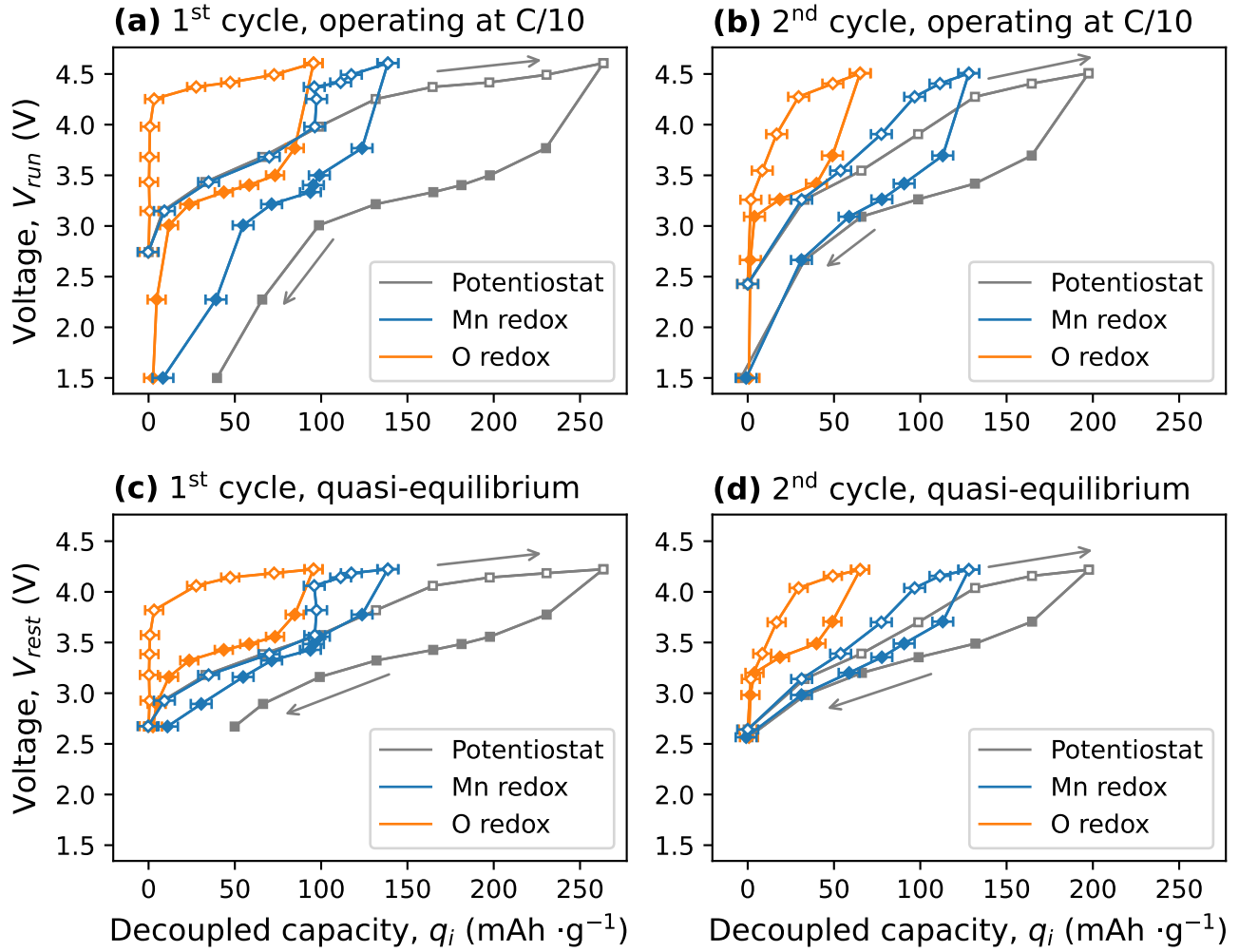
Figure 5: Decoupled redox voltage hysteresis for LMTO cathodes. (a) First-cycle operating voltage hysteresis, visualized by plotting operating voltages V_{run} against decoupled capacities q_i. C/10 rate $\equiv$ 0.1 mol e mol^{-1} h^{-1}. Operating voltages V_{run} were measured at cut-off points within constant-current cycles (SI Figure S8). (b) Second-cycle operating voltage hysteresis. (c) First-cycle quasi-static voltage hysteresis, visualized by plotting quasi-static voltages V_{rest} against decoupled capacities q_i. Quasi-static voltages V_{rest} were measured at relaxation endpoints of galvanostatic intermittent titration technique (GITT with 8 h relaxation between C/10 pulses, SI Figure S9). (d) Second-cycle quasi-static voltage hysteresis.

2.3.1 Operating Energy Efficiencies are Comparable

Operating voltage hysteresis is visualized by plotting operating voltage V_{run} vs. q_i (**Figure 5a, b**), where applied current is constant at 0.1 mol e mol^{-1} h^{-1} (**Figure S8**) and voltages were recorded at each cutoff before extraction for TiMS measurements. In the first charge, TiMS-decoupled Mn redox reveals two charging plateaus, with average voltages $\langle V_{run} \rangle$ = 3.50 V and 4.49 V. Upon discharge, Mn-redox voltage becomes sloped, so charge-discharge gaps vary within each plateau range: lower plateau with 0.48-1.61 V gaps; upper plateau with 0.76-0.88 V mismatch. The largest gap exceeds 1.6 V

in lower-plateau range having most Mn capacity, which drags down its round-trip energy efficiency to $\eta_{Mn} = 74.8\%$ — calculated from Equation (3), trapezoidal rule, and decoupled redox capacities. In contrast, first-cycle O redox shows $\langle V_{run} \rangle = 4.41$ V of a single charging plateau, (**Figure 5a**) whose V_{run} range is analogous to upper-plateau Mn redox. Unlike Mn-redox discharge curve, O redox shows a narrow discharging voltage at $\langle V_{run} \rangle = 3.37$ V. As a result, O-redox voltage gaps are more uniform with 0.78-1.29 V mismatch, and they are larger than upper-plateau Mn redox. However, a full charge-discharge cycle leads to similar deconvoluted efficiencies, ($\eta_O = 74.3\%$) which indicates that Mn redox and O redox have comparable impacts on the operating voltage hysteresis. That is, our DRX voltage hysteresis arises not just from O redox as the common culprit, but also from lower-plateau Mn redox. Because pure Mn redox shows similar hysteresis in a shallow-SOC cycle ($\eta_{Mn} = 71.6\%$ for blue line in **Figure 2a**), lower-plateau voltage hysteresis is probably not tied to upper-plateau O redox across the first full cycle. On the whole, as first-cycle q_{side} is non-zero, net energy efficiency η is further lowered to 67.1% at the end of first discharge.

Turning to the second cycle, both redox voltage profiles become more sloped. Unlike the first charge, Mn-redox plateaus become less separable with the two average voltages shifted down: lower-plateau $\langle V_{run} \rangle = 3.28$ V; higher-plateau $\langle V_{run} \rangle = 4.40$ V (**Figure 5b**). Furthermore, Mn-redox voltage profile display narrowed gaps at both lower plateau (0.53-0.93 V mismatch) and higher plateau (0.72-0.74 V mismatch). On the other hand, second-charge O redox starts earlier at 3.26 V than first-charge onset at 4.25 V, (**Figure 5a, b**) which leads to a wide V_{run} range and down-shifted voltage $\langle V_{run} \rangle = 4.10$ V on charging. Analogously, charge-discharge gaps decrease to 0.26-0.92 V for second-cycle O redox. Because both redox profiles show reduced voltage gaps, their second-cycle energy efficiencies increase to $\eta_{Mn} = 83.1\%$ and $\eta_O = 84.1\%$. Comparable efficiencies again implies that voltage hysteresis should not be ascribed to just one charge compensation mechanism, whether LMTO cathodes are in the first formation cycle or not. However, how each cycle achieves comparable redox efficiencies η_i remains unclear, as operating voltage hysteresis can arise from both thermodynamics and kinetics. Therefore, unfolding the origin of voltage hysteresis requires further quantitative decoupling between quasi-static (quasi-equilibrium) voltages and overvoltages.

2.3.2 Quasi-Static Energy Efficiencies and Overvoltages

To isolate kinetic overvoltage from operating voltage hysteresis, we applied galvanostatic intermittent titration technique with 8 h relaxation between 0.1C pulses, (GITT with $t_{rest} = 8$ h, 0.1C rate $\equiv$ 0.1

mol e mol^{-1} h^{-1}) as shown in **Figure S9**. Relaxation endpoints were recorded as quasi-static voltages V_{rest}, which form quasi-static voltage hysteresis in **Figure 5c, d**. As expected, V_{rest} curves show smaller charge-discharge mismatch than V_{run}, which leads to net quasi-static energy efficiencies η_0 greater than operating efficiencies η, such as first-cycle $\eta_0 = 74.2\%$ vs. $\eta = 67.1\%$. Analogously, deconvoluted redox efficiencies are higher in quasi-static hysteresis: first-cycle $\eta_{0,Mn} = 87.3\%$ and $\eta_{0,O} = 82.6\%$; second-cycle $\eta_{0,Mn} = 93.0\%$ and $\eta_{0,O} = 89.8\%$. Even though Mn redox and O redox have similar operating energy efficiencies $\eta_{Mn} \approx \eta_O$, their intrinsic efficiencies are different, with $\eta_{0,Mn} > \eta_{0,O}$ for both cycles. Comparison among $\eta_{0,i}$ and η_i suggests that two redox mechanisms have unequal overvoltages. In particular, Mn-redox V_{rest} curves almost overlap at first-cycle lower plateau, where operating Mn-redox hysteresis discloses the largest V_{run} gaps up to 1.61 V (**Figure 5a, c**). On the other hand, O redox does not show such large change from V_{rest} to V_{run}, with first-cycle gaps increased from 0.62 V to 1.04 V (averaged mismatch). Because O-redox V_{rest} and V_{run} curves share similar shape, O redox displays more uniform overvoltage distribution than Mn redox. Therefore, redox overvoltages scale each energy efficiency differently, from quasi-static to operating voltage hysteresis. To clarify operating hysteresis tied to each redox mechanism, we must quantify not only their overvoltage sizes, but also their overvoltage distribution.

Overvoltage distribution can be clearly visualized by plotting incremental capacities $\frac{|dq_i|}{dV}$ against V, where voltages are GITT-measured V_{run} or V_{rest} (**Figure 6**). Before analyzing V_{run} data, here we first focus on quasi-static V_{rest} distribution, as it sets starting points for developing overvoltages. Without overvoltage contribution, first-charge Mn redox displays bimodal V_{rest} distribution, while O redox have unimodal V_{rest} distribution (**Figure 6a, c**). First-discharge V_{rest} spreads across larger voltage windows than charge for both redox mechanisms. Turning to the second cycle, redox $\frac{|dq_i|}{dV_{rest}}$ peaks become flattened, which implies that DRX electronic band structure has both Mn and O orbital-energy levels broadened.[42] Widened distribution makes bimodal Mn-redox peaks overlapped, but O redox still has distinguishable and unimodal peaks. Although O-redox V_{rest} peak positions are separated for charge and discharge, upside-down peaks have almost identical shapes. Combining V_{rest} distribution with reversible selectivity S_i, (**Figure 6d, 4b**) our redox decoupling implies that the second charge involves up-shifting depopulated bands,[42] without much reshaping DRX band structure that underlies material's quasi-static behavior. Now with quasi-static $\frac{|dq_i|}{dV_{rest}}$ picturing LMTO voltage hysteresis close to its intrinsic limit, the overlaid $\frac{|dq_i|}{dV_{run}}$ further shows how voltage distribution deforms and shifts upon passing current.
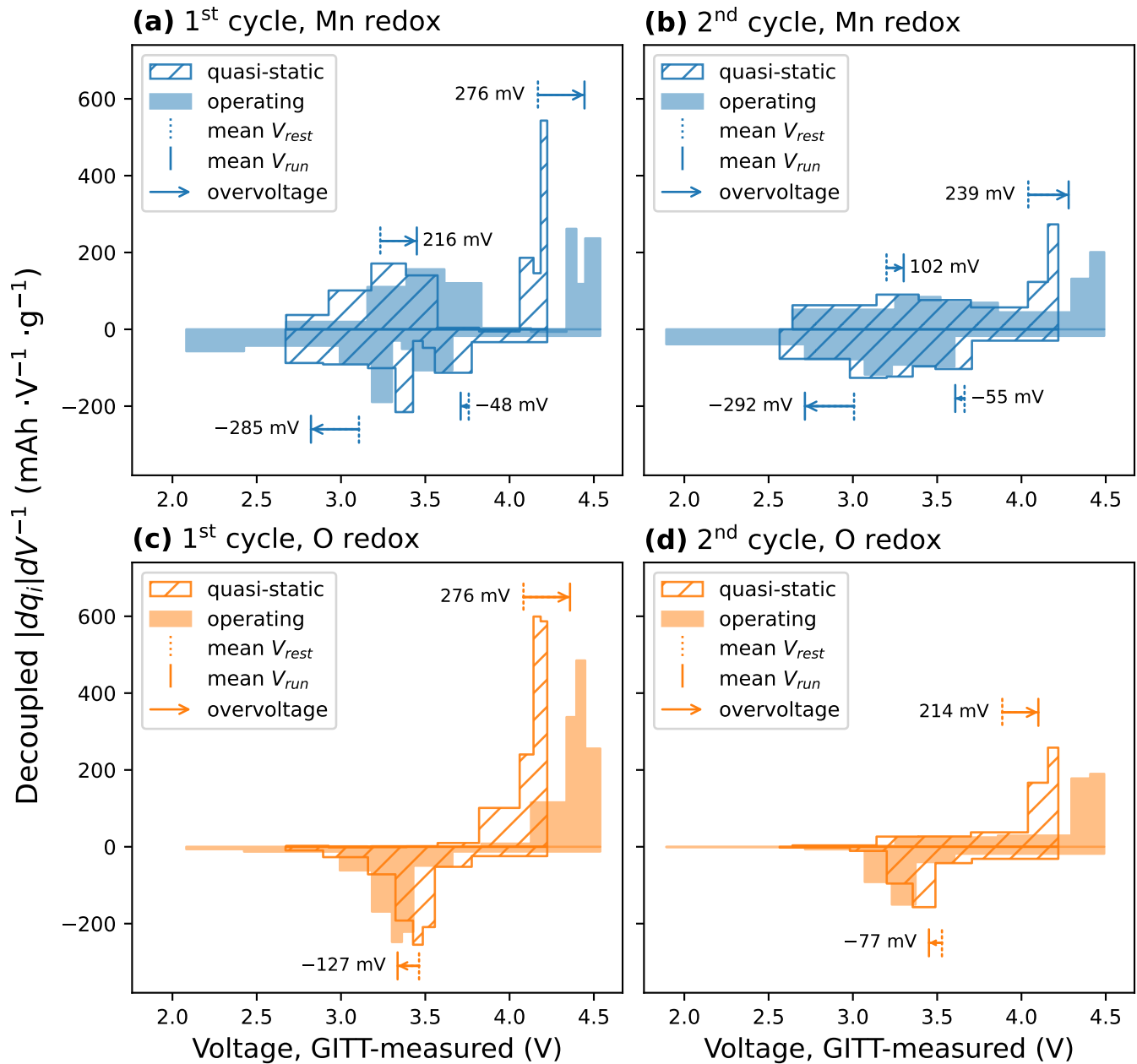
Figure 6: Deconvoluted voltage distribution and overvoltages for LMTO cathodes. (a) First-cycle Mn-redox incremental-capacity plot. Both quasi-static and operating voltages were GITT-measured (SI Figure S9). Mean V_{rest}, mean V_{run}, and overvoltages were derived from Equation (11). (b) Second-cycle Mn-redox incremental-capacity plot. (c) First-cycle O-redox incremental-capacity plot. (d) Second-cycle O-redox incremental-capacity plot.

With 0.1C current applied, both redox distributions shift nonuniformly along charge and discharge, which builds up asymmetric overvoltages. However, redox overvoltage magnitudes are challenging to quantify, as they not only vary across different capacity ranges, but also differ between Mn redox and O redox. To evaluate asymmetric redox overvoltages, we define mean overvoltage $\langle V_{over} \rangle_i$ as extra energy required for reaction coordinates that compensate a unit electric charge via a redox-active species i,

averaged over a decoupled capacity range Q:

$$\langle V_{over}\rangle_i \equiv \frac{\displaystyle\int_Q V_{run}dq_i - \int_Q V_{rest}dq_i}{\displaystyle\int_Q dq_i} = \langle V_{run}\rangle_i - \langle V_{rest}\rangle_i \tag{11}$$

A natural outcome is that mean redox overvolage equals mean difference between operating and quasi-static redox voltages, which are positioned by vertical bars in **Figure 6**. Mn-redox overvoltages are evaluated separately in each plateau q_{Mn} range (two charge-discharge $\langle V_{over}\rangle_{Mn}$ pairs). Lower-V Mn redox has larger discharging overvoltage than charging, while charge-discharge comparative is flipped for the higher-V range. In particular, higher-V charging overvolages are similar for both Mn and O redox, which implies their relevance during higher-V charging. Because charging q_O is greater than q_{Mn} at the higher-V range, charging $\langle V_{over}\rangle_O$ is larger than $\langle V_{over}\rangle_{Mn}$ averaged across the entire charge range, e.g., $\langle V_{over}\rangle_O = 276$ mV and $\langle V_{over}\rangle_{Mn} = 234$ mV throughout the first charge. On the contrary, discharging $\langle V_{over}\rangle_O$ is smaller than $\langle V_{over}\rangle_{Mn}$ across the whole discharge range, e.g., $\langle V_{over}\rangle_O = -127$ mV and $\langle V_{over}\rangle_{Mn} = -201$ mV all over the first discharge. Furthermore, from the first to the second cycle, most of overvoltages improve, but only discharging $\langle V_{over}\rangle_{Mn}$ remains similar, which upholds kinetic limitation by Mn redox. Larger Mn-redox overvoltages imply that O redox does not necessarily limit DRX-like materials' kinetic performance, which answers why ultrahigh rate capability can be achieved by materials exhibiting mixed Mn and O redox.[43] To summarize, our overvoltage decoupling indicates that LMTO cathode has variable kinetic constraints: in mixed redox contribution range, excess charging energy is dominated by O redox; across entire capacity range, accessible discharging energy is predominantly limited by Mn redox. Even though Mn redox has higher quasi-static energy efficiency than O redox, LMTO operating energy efficiency is largely dragged down by Mn-redox discharging overvoltage.

3 Conclusion and Broader Context

In conclusion, LMTO voltage hysteresis arises not only from intrinsic charge-discharge voltage mismatch of O redox, but also from asymmetric Mn-redox overvoltages. Along deconvoluted hysteresis curves in the capacity dimension, our two-step titration mass spectrometry can quantify Mn and O redox capacities separately, which display their reversibility in decoupled coulombic efficiency close to 100%. Our decoupling results indicate the most effective strategy to lower net irreversible capacity for future

DRX materials: suppressing interface side reactions during the first formation cycle. Beyond LMTO's first cycle, our technique reveals reversible faradaic selectivity between two intermixed redox mechanisms. With redox capacities quantified incrementally, we can evaluate redox voltage hysteresis via deconvoluted energy efficiencies η_i. High quasi-static $\eta_{0,Mn}$ up to 93% shows promise of developing high-efficiency DRX materials, which should focus on improving discharging overvoltages that drag operating η_{Mn} down to 83%. Therefore, we anticipate that our unique analytical workflow can diagnose various DRX materials and inform improvement direction, as diverse design strategies have been developed and proved effective, e.g., fluorination,[44] high-entropy TM chemistry,[45] synthetic optimization,[9] and partial spinel order.[43] With proper diagnosis and advancement in DRX materials' enormous design space, we envision that future DRX cathodes may not only feature low cost and high energy density, but also achieve high energy efficiency, which is particularly critical for EV batteries in electrifying transportation. As power grids transition from fossil fuel to sustainable energy at a slow pace, future EV cells must have high energy efficiency to further reduce equivalent CO_2 emission per mile, which thus warrants our in-depth study on the emerging DRX cathode's voltage hysteresis.

4 Experimental Section

Material synthesis: Cation-disordered rock salt $Li_{1.2}Mn_{0.4}Ti_{0.4}O_2$ (LMTO) was synthesized by a traditional solid-state method. Li_2CO_3 (Sigma, 99%), Mn_2O_3 (Alfa Aesar, 99.9%) and TiO_2 (Alfa Aesar, 99.9%) were used as precursors. All the precursors were stoichiometrically mixed in ethanol with a Retsch PM 200 planetary ball mill at a rate of 250 rpm for 12 h. 10% excess Li_2CO_3 was added to compensate for possible loss during synthesis at high temperature. The precursors were then dried in an oven at 70°C overnight and pelletized. The precursor pellets were heated to 1100°C at a rate of 9 °C min^{-1} under Ar gas flow and held for 20 min followed by cooling naturally in the furnace. To ensure long-range phase purity, lab X-ray diffraction patterns (SI **Figure S3**) were examined using a Rigaku Miniflex 600 in the 2θ range of 15–90°. Rietveld refinement was performed using PANalytical X'pert HighScore Plus software.

Pourbaix diagram: To promote the aqueous instability of solid-phase $Mn^{3+/4+}$ in acid solution, we referred to a computed Pourbaix diagram[30] of cation-ordered $LiMn_2O_4$. Spinel $LiMn_2O_4$ pourbaix diagram was generated through open-source Python Materials Genomics (pymatgen)[46] packages. To predict solid-aqueous equilibria, the computation adopts a formalism[31] aligning experimentally

tabulated aqueous-state free energies with ab initio calculated solid-state energies, which were acquired via accessing Materials Project database.[33] As the database is actively updated, we observed slight variation in reproducing converged energy values, but their resulting Pourbaix diagram's pattern did not change. All aqueous ion concentrations were set at 10^{-6} M. Composition of metal elements is Li:Mn = 1:2, which follows unit formula of $LiMn_2O_4$ (Material ID: mp-22584). Instability map was computed from initial $LiMn_2O_4$ (s) free energy relative to equilibria-predicted states, which takes H^+ (aq), OH^- (aq), H_2O (l), and electrons into account.[32]

Electrochemical cell assembly: To monitor in-situ gas evolution associated with interface parasitic reaction and O_2 loss, we measured all LMTO cathodes' voltages and net capacities in a modified Swagelok-type cell format.[47] Cathodes were prepared in a Ar-filled glove box to limit their exposure to the ambient. LMTO powder was first mortar-milled with carbon black (Super C65, TIMCAL) in 7:2 weight ratio for 30 minutes. Milled LMTO-carbon powder was then mixed with polyvinylidene fluoride (Solef 6010/1001, SOLVAY) solution in N-Methyl-2-pyrrolidone solvent (NMP, anhydrous, 99.5%, Sigma Aldrich) to form slurry in a planetary centrifugal mixer (ARE-310, THINKY Mixer). Additional conductive carbon (Super P, TIMCAL) and NMP were added to expand slurry to an adequate volume that enables uniform mixing in the mixer container (6 mL polypropylene container). Final solid weight composition becomes 62% active material, 28% carbon, and 10% binder. Slurry was cast onto a stainless-steel mesh, (120 mesh, T-316 stainless steel, TWP inc.) which allows gas to escape in cell axial direction. After drying on a 120°C hot plate for an hour, the electrode was cut into 12 mm discs. Cathode discs were further dried overnight under static vacuum at 120°C in a heated antechamber attached to the glove box. The loading density ranged between 4.5-7.0 mg cm^{-2} for the cathode active material. Cell anodes are lithium disks in 12 mm diameter (FMC). To avoid short circuit in each Swagelok-type cell, two layers of membrane were used as the separator: a quartz microfiber disc (Whatman QM-A, cytiva) facing the cathode; a polypropylene film (Celgard 2500) facing the anode. All cell components were wet with 80 μL of 1 M $LiPF_6$ (Gotion) in EC/DEC (BASF, 1:1 v/v) in each cell, and they were assembled in the glove box. Constant-current experiments were tested under ambient temperature (ranged between 22-28°C), while galvanostatic intermittent titration technique (GITT, SI **Figure S9**) was carried out in a 30°C chamber (Thermotron).

Differential electrochemical mass spectrometry: We quantified in-situ gas evolution rate via a custom-built system handling gas flow from electrochemical cells to a mass-spectrometry (MS) gas

analyzer, which is commonly called differential electrochemical mass spectrometry (DEMS).[47] MS signals are calibrated for O_2 (research grade, Linde) and CO_2 (> 99.9%, Linde) in Ar carrier gas (ultra-high purity, Linde). To avoid interference from the ambient air, each DEMS cell was leak-tested before the measurement began. A Bio-Logic VSP-series potentiostat was used to control the current passed through the DEMS cell, while voltages and net electric charge transfer were recorded every 20 seconds. Every 10 minutes, accumulated gas in each cell headspace ($\sim$100 µL) was purged intermittently using 500 µL pulses of Ar at recorded gas pressures and room temperatures. In-situ evolved gas was sent to a holding chamber, where a variable leak valve controls sampled gas flow into a ultrahigh-vacuum chamber for MS analysis.

Titration mass spectrometry: To quantify characteristic gas products from analyte-titrant reactions, we custom-made a three-neck glass vessel that can be sealed and attached to a gas-handling system along with a MS gas analyzer, which is similar to DEMS and was named titration mass spectrometry (TiMS).[28] Each glass vessel has two necks, as gas inlet and outlet, connected to the gas-handling system via a combination of Ace-Thred adapters (Ace Glass Inc.), perfluoroalkoxy tubes, and Valco column end fittings (VICI AG.). The third glass neck was septum-sealed, (#7 Ace-Thred, 5037-30) which serves as a titrant injection port. Before each titration experiment, cycled cathodes were extracted from DEMS cells in the Ar-filled glove box, rinsed with 350 µL dimethyl carbonate (Gotion) for three times, and dried at room temperature under vacuum for >1 h to remove residual electrolyte. Each dried cathode was sealed into a titration glass vessel in the glove box to limit their exposure to the ambient. After attaching the vessel to the TiMS system, we leak-tested and purged the vessel with Ar carrier gas to avoid interference from the ambient air. All titrants were Ar-sparged for >2 h to remove residual air dissolved in the aqueous solution. A gas-tight syringe (VICI, Series C syringe with Pressure-Lok side port needle) was used to inject titrant solution, as this syringe design can avoid introducing any air into the vessel upon injection. Meanwhile, we continuously monitored vessel gas composition via MS gas analyzer to ensure that no air (MS signals: m/z = 14, 28, 32) was introduced during the injection. To destabilize solid-phase oxidized oxygen, we injected 1.5 mL of strong acid titrant, 1 M triflic acid (HSO_3CF_3 (aq)), which was selected due to its extremely negative pKa and its stable anion chemistry. After O_2 evolution was attenuated, we injected 4.5 mL of 0.75 M $H_2C_2O_4$ + 0.05 M HSO_3CF_3 (aq) to reduce solid-phase $Mn^{3+/4+}$, which induces oxalate-CO_2 evolution. Gas accumulated in the vessel headspace ($\sim$5 mL) was purged by 2 mL of pulsed Ar every 2 minutes (one-channel system) or 4 minutes (two-channel system). A longer time interval between Ar pulses leads to a wider residence-time distribution of gas in the vessel

headspace, but it does not change the net amount of gas collected (the area below each curve), which explains the difference of curve shapes in **Figure 3b**. All swept-out gas samples was subsequently quantified by the MS gas analyzer.

Supporting Information

Supporting Information is available from the Wiley Online Library or from the author.

References

[1] W. Li, E. M. Erickson, A. Manthiram, *Nature Energy* **2020**, *5*, 1 26.

[2] W. Heijlen, G. Franceschi, C. Duhayon, K. Van Nijen, *Resources Policy* **2021**, *73* 102202.

[3] X. Fu, D. N. Beatty, G. G. Gaustad, G. Ceder, R. Roth, R. E. Kirchain, M. Bustamante, C. Babbitt, E. A. Olivetti, *Environmental Science & Technology* **2020**, *54*, 5 2985.

[4] Z. Yang, H. Huang, F. Lin, *Advanced Energy Materials* **2022**, 2200383.

[5] J. Lee, A. Urban, X. Li, D. Su, G. Hautier, G. Ceder, *Science* **2014**, *343*, 6170 519.

[6] N. Yabuuchi, M. Takeuchi, M. Nakayama, H. Shiiba, M. Ogawa, K. Nakayama, T. Ohta, D. Endo, T. Ozaki, T. Inamasu, K. Sato, S. Komaba, *Proceedings of the National Academy of Sciences of the United States of America* **2015**, *112*, 25 7650.

[7] R. Chen, S. Ren, M. Knapp, D. Wang, R. Witter, M. Fichtner, H. Hahn, *Advanced Energy Materials* **2015**, *5*, 9 1.

[8] H. Ji, A. Urban, D. A. Kitchaev, D. H. Kwon, N. Artrith, C. Ophus, W. Huang, Z. Cai, T. Shi, J. C. Kim, H. Kim, G. Ceder, *Nature Communications* **2019**, *10*, 1.

[9] Z. Cai, Y. Zhang, Z. Lun, B. Ouyang, L. C. Gallington, Y. Sun, H. Hau, Y. Chen, M. C. Scott, G. Ceder, *Advanced Energy Materials* **2022**, 2103923.

[10] R. J. Clément, Z. Lun, G. Ceder, *Energy & Environmental Science* **2020**, *13* 345.

[11] A. Abdellahi, A. Urban, S. Dacek, G. Ceder, *Chemistry of Materials* **2016**, *28*, 15 5373.

[12] K. McColl, R. A. House, G. J. Rees, A. G. Squires, S. W. Coles, P. G. Bruce, B. J. Morgan, M. S. Islam, *Nature Communications* **2022**, *13*, 1 5275.

[13] R. Sharpe, R. A. House, M. J. Clarke, D. Förstermann, J.-J. Marie, G. Cibin, K.-J. Zhou, H. Y. Playford, P. G. Bruce, M. S. Islam, *Journal of the American Chemical Society* **2020**, *142*, 52 21799.

[14] D. H. Seo, J. Lee, A. Urban, R. Malik, S. Kang, G. Ceder, *Nature Chemistry* **2016**, *8*, 7 692.

[15] N. Yabuuchi, M. Nakayama, M. Takeuchi, S. Komaba, Y. Hashimoto, T. Mukai, H. Shiiba, K. Sato, Y. Kobayashi, A. Nakao, M. Yonemura, K. Yamanaka, K. Mitsuhara, T. Ohta, *Nature Communications* **2016**, *7* 1.

[16] R. A. House, G. J. Rees, M. A. Pérez-Osorio, J. J. Marie, E. Boivin, A. W. Robertson, A. Nag, M. Garcia-Fernandez, K. J. Zhou, P. G. Bruce, *Nature Energy* **2020**, *5*, 10 777.

[17] I. I. Abate, C. D. Pemmaraju, S. Y. Kim, K. H. Hsu, S. Sainio, B. Moritz, J. Vinson, M. F. Toney, W. Yang, W. E. Gent, T. P. Devereaux, L. F. Nazar, W. C. Chueh, *Energy & Environmental Science* **2021**, *14*, 9 4858.

[18] R. A. House, U. Maitra, M. A. Pérez-Osorio, J. G. Lozano, L. Jin, J. W. Somerville, L. C. Duda, A. Nag, A. Walters, K. J. Zhou, M. R. Roberts, P. G. Bruce, *Nature* **2020**, *577*, 7791 502.

[19] Y. Yue, Y. Ha, T.-Y. Huang, N. Li, L. Li, Q. Li, J. Feng, C. Wang, B. D. McCloskey, W. Yang, W. Tong, *ACS Nano* **2021**, *15*, 8 13360.

[20] J. Hong, W. E. Gent, P. Xiao, K. Lim, D.-H. Seo, J. Wu, P. M. Csernica, C. J. Takacs, D. Nordlund, C.-J. Sun, K. H. Stone, D. Passarello, W. Yang, D. Prendergast, G. Ceder, M. F. Toney, W. C. Chueh, *Nature Materials* **2019**, *18*, 3 256.

[21] B. Qiu, M. Zhang, S.-Y. Lee, H. Liu, T. A. Wynn, L. Wu, Y. Zhu, W. Wen, C. M. Brown, D. Zhou, Z. Liu, Y. S. Meng, *Cell Reports Physical Science* **2020**, *1*, 3 100028.

[22] B. Li, M. T. Sougrati, G. Rousse, A. V. Morozov, R. Dedryvère, A. Iadecola, A. Senyshyn, L. Zhang, A. M. Abakumov, M.-L. Doublet, J.-M. Tarascon, *Nature Chemistry* **2021**, *13*, 11 1070.

[23] N. Birkner, S. Nayeri, B. Pashaei, M. M. Najafpour, W. H. Casey, A. Navrotsky, *Proceedings of the National Academy of Sciences* **2013**, *110*, 22 8801.

[24] S. Ramakrishnan, B. Park, J. Wu, W. Yang, B. D. McCloskey, *Journal of the American Chemical Society* **2020**, *142*, 18 8522.

[25] M. J. Crafton, Y. Yue, T.-Y. Huang, W. Tong, B. D. McCloskey, *Advanced Energy Materials* **2020**, *10*, 35 2001500.

[26] E. Billy, M. Joulié, R. Laucournet, A. Boulineau, E. De Vito, D. Meyer, *ACS Applied Materials & Interfaces* **2018**, *10*, 19 16424.

[27] A. A. Frost, *Journal of the American Chemical Society* **1951**, *73*, 6 2680.

[28] T.-Y. Huang, M. J. Crafton, Y. Yue, W. Tong, B. D. McCloskey, *Energy & Environmental Science* **2021**, *14*, 3 1553.

[29] C. J. Ballhausen, *Introduction to Ligand Field Theory*, McGraw-Hill series in advanced chemistry. McGraw-Hill Book Company, Inc., New York, **1962**.

[30] W. T. Thompson, M. H. Kaye, C. W. Bale, A. D. Pelton, In *Uhlig's Corrosion Handbook.* (Ed: R. W. Revie), John Wiley & Sons, Hoboken, New Jersey, **2011**, Ch. 8.

[31] K. A. Persson, B. Waldwick, P. Lazic, G. Ceder, *Physical Review B - Condensed Matter and Materials Physics* **2012**, *85*, 23 235438.

[32] A. K. Singh, L. Zhou, A. Shinde, S. K. Suram, J. H. Montoya, D. Winston, J. M. Gregoire, K. A. Persson, *Chemistry of Materials* **2017**, *29*, 23 10159.

[33] A. M. Patel, J. K. Nørskov, K. A. Persson, J. H. Montoya, *Physical Chemistry Chemical Physics* **2019**, *21*, 45 25323.

[34] S. E. Renfrew, B. D. McCloskey, *ACS Applied Energy Materials* **2019**, *2*, 5 3762.

[35] R. Jung, M. Metzger, F. Maglia, C. Stinner, H. A. Gasteiger, *Journal of The Electrochemical Society* **2017**, *164*, 7 A1361.

[36] L. A. Kaufman, B. D. McCloskey, *Chemistry of Materials* **2021**, *33*, 11 4170.

[37] B. L. D. Rinkel, J. P. Vivek, N. Garcia-Araez, C. P. Grey, *Energy & Environmental Science* **2022**.

[38] D.-H. Kwon, J. Lee, N. Artrith, H. Kim, L. Wu, Z. Lun, Y. Tian, Y. Zhu, G. Ceder, *Cell Reports Physical Science* **2020**, *1*, 9 100187.

[39] J. Reed, G. Ceder, *Chemical Reviews* **2004**, *104*, 10 4513.

[40] K. Dai, W. Shao, B. Zhao, W. Zhang, Y. Feng, W. Mao, G. Ai, G. Liu, J. Mao, W. Yang, *Journal of Energy Chemistry* **2022**, *69* 363.

[41] A. Grenier, P. J. Reeves, H. Liu, I. D. Seymour, K. Märker, K. M. Wiaderek, P. J. Chupas, C. P. Grey, K. W. Chapman, *Journal of the American Chemical Society* **2020**, *142*, 15 7001.

[42] M. Okubo, A. Yamada, *ACS Applied Materials & Interfaces* **2017**, *9*, 42 36463.

[43] H. Ji, J. Wu, Z. Cai, J. Liu, D.-H. Kwon, H. Kim, A. Urban, J. K. Papp, E. Foley, Y. Tian, M. Balasubramanian, H. Kim, R. J. Clément, B. D. McCloskey, W. Yang, G. Ceder, *Nature Energy* **2020**, *5*, 3 213.

[44] B. Ouyang, N. Artrith, Z. Lun, Z. Jadidi, D. A. Kitchaev, H. Ji, A. Urban, G. Ceder, *Advanced Energy Materials* **2020**, *10*, 10 1.

[45] Z. Lun, B. Ouyang, D.-H. Kwon, Y. Ha, E. E. Foley, T.-Y. Huang, Z. Cai, H. Kim, M. Balasubramanian, Y. Sun, J. Huang, Y. Tian, H. Kim, B. D. McCloskey, W. Yang, R. J. Clément, H. Ji, G. Ceder, *Nature Materials* **2021**, *20*, 2 214.

[46] S. P. Ong, W. D. Richards, A. Jain, G. Hautier, M. Kocher, S. Cholia, D. Gunter, V. L. Chevrier, K. A. Persson, G. Ceder, *Computational Materials Science* **2013**, *68* 314.

[47] B. D. McCloskey, D. S. Bethune, R. M. Shelby, G. Girishkumar, A. C. Luntz, *The Journal of Physical Chemistry Letters* **2011**, *2*, 10 1161.